

Doping dependence of electronic structure of infinite-layer NdNiO₂

Zhao Liu^{1,2}, Chenchao Xu^{2,3}, Chao Cao^{3,*}, W. Zhu², Z. F. Wang¹ and Jinlong Yang^{1,†}

¹Hefei National Laboratory for Physical Sciences at the Microscale, University of Science and Technology of China, Hefei, Anhui 230026, China

²Key Laboratory for Quantum Materials of Zhejiang Province, School of Science, Westlake University, 18 Shilongshan Road, Hangzhou 310024, China

³Hangzhou Key Laboratory of Quantum Matter, Hangzhou Normal University, Hangzhou 310036, China



(Received 21 September 2020; revised 7 December 2020; accepted 14 December 2020; published 4 January 2021)

We investigate the electronic structure of nickelate superconductor NdNiO₂ upon hole doping, by means of density-functional theory and dynamical mean-field theory. We demonstrate the strong intrinsic hybridization between strongly correlated states formed by Ni-3d_{x²-y²} orbital and itinerant electrons due to Nd-5d and Ni-3d_{z²} orbitals, producing a valence-fluctuating correlated metal as the normal state of hole-doped NdNiO₂. The Hund's rule appears to play a dominating role on multiorbital physics in the lightly doped compound, while its effect is gradually reduced by increasing the doping level. Crucially, the hole-doping leads to intricate effects on Ni-3d orbitals, such as a nonmonotonic change of electron occupation in lightly doped level, and a flipping orbital configuration in the overdoped regime. Additionally, we also map out the topology of Fermi surface at different doping levels. These findings render a preferred window to peek into electron pairing and superconductivity.

DOI: [10.1103/PhysRevB.103.045103](https://doi.org/10.1103/PhysRevB.103.045103)

I. INTRODUCTION

Recent discovery of superconductivity in hole-doped infinite-layer NdNiO₂ adds the nickelate material to the family of unconventional superconductivity [1]. While the crystal structure of NdNiO₂ is similar to the infinite-layer copper oxide superconductors, the electronic structure and magnetic properties of NdNiO₂ are very different, which triggers intense on-going discussion. Especially, the O-2p states are deeply below the Fermi level, which points to a Mott insulator for NdNiO₂ [2–5]. The strong insulating behavior is suppressed by the self-doping effect due to hybridization between Nd-5d conduction electrons and Ni-3d local orbitals [6,7], producing a bad metal observed in transport measurements. Additionally, the related magnetic properties can be understood within the similar route [8–12]. Besides these studies on the parent compound, the microscopic origin for superconductivity is still elusive [13–19]. Since the nature of normal state may be responsible for electron pairing and superconductivity, it is important to determine their charge doping evolution and connection with superconductivity [20–22].

Let us recall the effect of hole doping on the well-known copper oxide superconductors where Cu-3d local orbitals is mediated by the O-2p orbitals. A consequence is that upon hole doping most of holes reside on the O-2p orbitals [23]. The holes in O-2p orbitals will largely weaken the antiferromagnetic ordering and induce strong magnetic fluctuations, driving the system into d-wave superconductivity [24,25]. Moreover, since the spins on O-2p orbitals strongly interact

with local spin on Cu-3d states and form the Cu-O spin singlet (Zhang-Rice state) [26], a single-band *t*-*J* model is believed to capture essential physics in cuprates [27]. Since the dynamics of holes play an important role in possible mechanism for superconductivity in cuprates, it immediately raises questions: Does the hole doping play a similar role in NdNiO₂? If not, what is the nature of normal state of hole-doped NdNiO₂?

To address these questions, one needs the electron occupation and spin information on multiorbitals using unbiased computations. Despite extensive investigations [28–38], many open issues still remains, waiting for critical justification. For example, the hole doping is usually simulated by the shifts of the energy bands [40]; nevertheless, the possible electronic state induced by doping Sr has not been well addressed. Moreover, to avoid the discussion of *f* electrons on neodymium [39], most of existing literatures made a detour and studied LaNiO₂ alternatively, but these calculations are at odds with the experimental fact that no superconductivity is found in LaNiO₂ [1]. In a word, a full-electron *ab initio* simulation of hole-doped NdNiO₂ is still outstanding.

In this work, we aim at the normal state of NdNiO₂ by performing both density functional theory (DFT) and dynamical mean field theory (DMFT) calculations. First, we build a realistic doping model to study the effect of Sr doping continuously and find that the evolution of the electronic states upon hole doping is nonrigid band like: The electron pocket at Γ point vanishes quickly, and the Fermi level is almost pinned by the Ni-3d_{x²-y²} orbital. Then we perform a many-body calculation on the normal state of hole-doped NdNiO₂ without considering the *f* orbitals and compare with the results from full electron many-body calculations by explicitly considering Nd-4*f* electrons. We identify several key features in the evolution of electronic structure upon hole doping: (1) While

*ccaao@hznu.edu.cn

†jlyang@ustc.edu.cn

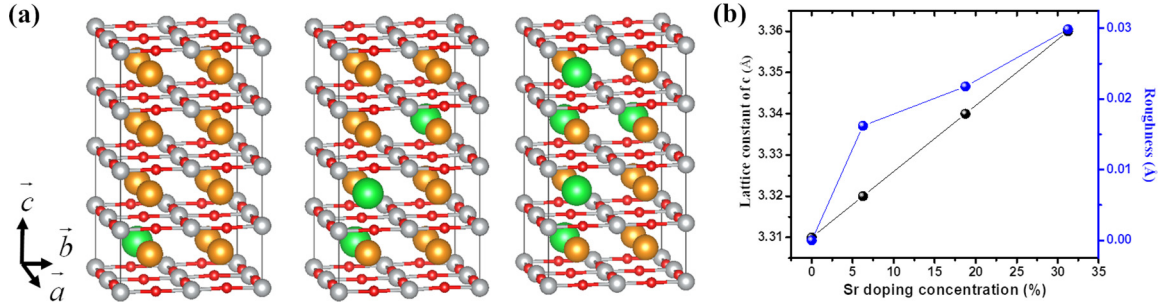


FIG. 1. (a) From left to right: perspective view of NdNiO₂ supercell with $\delta = 6.25\%$, 18.75% , and 31.25% . The silver, red, yellow, and green balls represent Ni, O, Nd, and Sr atoms. (b) Lattice constant in *c* direction and roughness with respect to δ .

the d^9 state is the most probable, the weight of d^8 is much larger than $d^{10}\underline{L}$ (\underline{L} means a hole on ligand), which points to a multiorbital physics rather than the charge-transfer picture; (2) the total occupation of Ni-3*d* state is close to 8.6, and thus a lightly doped compound is a valence-fluctuating correlated metal; (3) the Hund's rule plays an important role in the lightly doped compound, and its effect is gradually reduced upon hole doping; (4) there is a nonmonotonic doping effect in Ni-3*d* orbital configuration; (5) significant band renormalization is observed for the Ni-3*d*_{*x*²-*y*²} state, with mass enhancement of ≈ 2.4 . It is quickly suppressed to ≈ 2.1 upon heavy hole doping. We believe these findings are helpful to understand the unconventional superconductivity in this system. For instance, the correlated Ni-3*d*_{*x*²-*y*²} orbital is most relevant for electron pairing, and the change of topology of Fermi surface could result in disappearance of superconductivity.

II. METHODS

A. DFT calculations

DFT calculation was performed with the plane wave projector augmented wave method implemented in the Vienna *ab initio* simulations package (VASP) [41–43]. The Perdew-Burke-Ernzerhof version of generalized gradient approximation (PBE) was applied [44]. To simulate the effect of Sr doping, one, three, and five Nd atoms are replaced by Sr atoms in a $2 \times 2 \times 4$ supercell containing 16 Nd, 16 Ni, and 32 O atoms, as depicted in Fig. 1(a). In this way, we can consistently mimic the hole doping concentration (δ) at 6.25%, 18.75%, and 31.25% lying at the underdoped, optimal doping, and overdoped regions [20,21]. Considering the fact that the thin films are grown on the SrTiO₃ (001) surface, the lattice constants in the *ab* plane of supercell cell are fixed to $a = b = 3.92$ Å while the lattice constant in the *c* direction and atomic positions are allowed to relax. For band structure calculation, we choose the following high symmetric path: $\Gamma(0, 0, 0)$ -X($\pi, 0, 0$)-M($\pi, \pi, 0$)- Γ -Z($0, 0, \pi$)-R($\pi, 0, \pi$)-A(π, π, π)-Z [see Fig. 2(a)]. To show the effect of Sr doping on electronic structures, all the band structures are unfolded to the unit cell with the PYPROCAR package [45].

B. DFT+DMFT calculations

DFT + DMFT calculations were performed using the code EDMFT, developed by Haule *et al.* [46] based on the WIEN2K package [47]. Similar to prior studies, we replace Nd with

La in our calculations, and the doping effect is simulated by removing conduction electrons in the spirit of virtual crystal approximation (VCA) [48]. Charge self-consistency is enforced throughout the calculations. The on-site Coulomb interaction parameters for Ni-3*d* orbitals are chosen to be $F^0 = 6.0$ eV, $F^2 = 7.754$ eV, and $F^4 = 4.846$ eV, respectively, or equivalently $U = 6.0$ eV and $J = 0.9$ eV. We employ nominal double-counting $V_{dc} = U(n_d^0 - 1/2) - J/2(n_d^0 - 1)$ with $n_d^0 = 9$. The local impurity problem is solved using continuous-time quantum Monte Carlo (CTQMC) method [49] at $\beta = 100$ eV⁻¹ or 116 K. For each impurity problem, we used 4×10^9 total CTQMC steps in each DMFT iteration, and self energies from the last five iterations after convergence were averaged and analytically continued to obtain real-frequency self-energy $\Sigma(\omega)$ using the maximum entropy method.

III. RESULTS

A. DFT results

We first calculate the lattice constant in the *c* direction [see Fig. 1(b)] and observe a linear relation between Sr doping concentration and *c*, in accordance with experimental results [20]. After structural optimization, the NiO₂ plane is no longer exactly flat as in the pristine compound. To measure the roughness of the plane, we define roughness as $R = \max\{\delta_c\}$, where δ_c is the buckling of each NiO₂ plane in the supercell (in unit of Å). As displayed in Fig. 1(b), *R* is less than 0.03 Å even at large $\delta = 31.25\%$, and therefore the effect of structure distortion on electronic structure is secondary, making it possible to prepare the atomically flat surface for scanning tunneling microscopy [22].

The unfolded band structures at different δ are shown in Figs. 2(a)–2(d), where the band structure of the pristine compound is also plotted to guide the eye. To facilitate our discussion, we label the Fermi pockets as α , β , and γ for the dominating sheet, pocket at Γ point, and pocket at A point in the pristine compound [8,22]. These pockets behave differently than with Sr doping. Among these Fermi pockets, the β pocket is very sensitive to Sr doping and almost vanishes at a low doping level $\delta = 6.25\%$. Since it is contributed by Nd d_{z^2} and Ni d_{z^2} orbitals, their densities of states (DOS) gradually decrease to zero as shown in Figs. 2(e) and 2(h). When δ increases to 31.25%, the β pocket has experienced a blue shift up to 0.86 eV. Such a large shift indicates the free-particle nature of this pocket. The γ pocket, which has

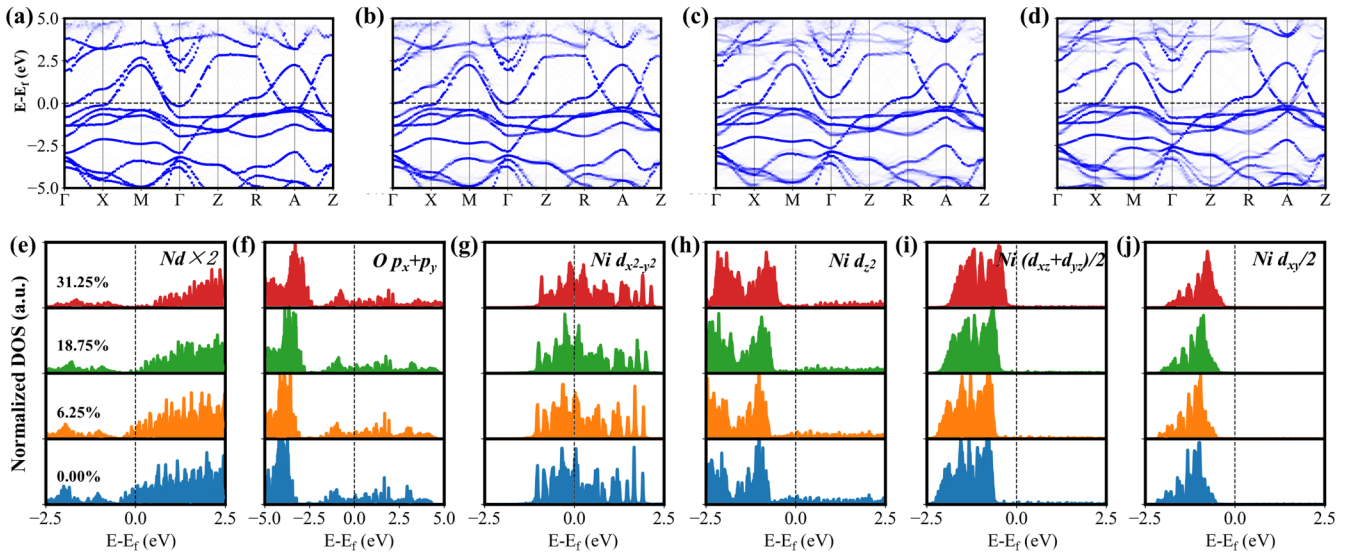


FIG. 2. [(a)–(d)] Unfolded band structures for different Sr doping concentration. From left to right: $\delta = 0.00\%$, 6.25% , 18.75% , and 31.25% . [(e)–(j)] Projected density of state with different δ on different subspaces with arbitrary unit (a.u.), from left to right: Nd atoms, O p_{x+y} orbitals, Ni $d_{x^2-y^2}$ orbitals, Ni d_{z^2} orbitals, Ni $d_{xz} + d_{yz}$ orbitals, and Ni d_{xy} orbitals. The weights in panels (e), (i), and (j) have been rescaled by factors of 2, 1/2, and 1/2. From bottom to top, δ increases from 0.00% to 31.25% in each figure.

smaller effective electron mass and thus is more itinerant, nevertheless has smaller blue shift than the β pocket and does not vanish even at $\delta = 31.25\%$. In a free-particle picture, homogeneous hole doping will lead to the drop of Fermi level, namely, all the bands become rigid and have the same blue shift. The smaller blue shift of the more itinerant γ pocket reflects that such a pocket is actually more correlated. As we

will show below, such a correlation originates from the Hund's coupling between Ni-3d for this pocket is mainly formed by the Ni d_{xz} and d_{yz} orbitals [8]. As for the α sheet, its blue shift strongly depends on δ . At smaller δ , it does not shift until the vanishing of β pocket [see Fig. 2(g)]. After that, it slowly undergoes blue shift together with γ pocket. Moreover, since the α sheet wraps around a large volume, its blue shift is quite

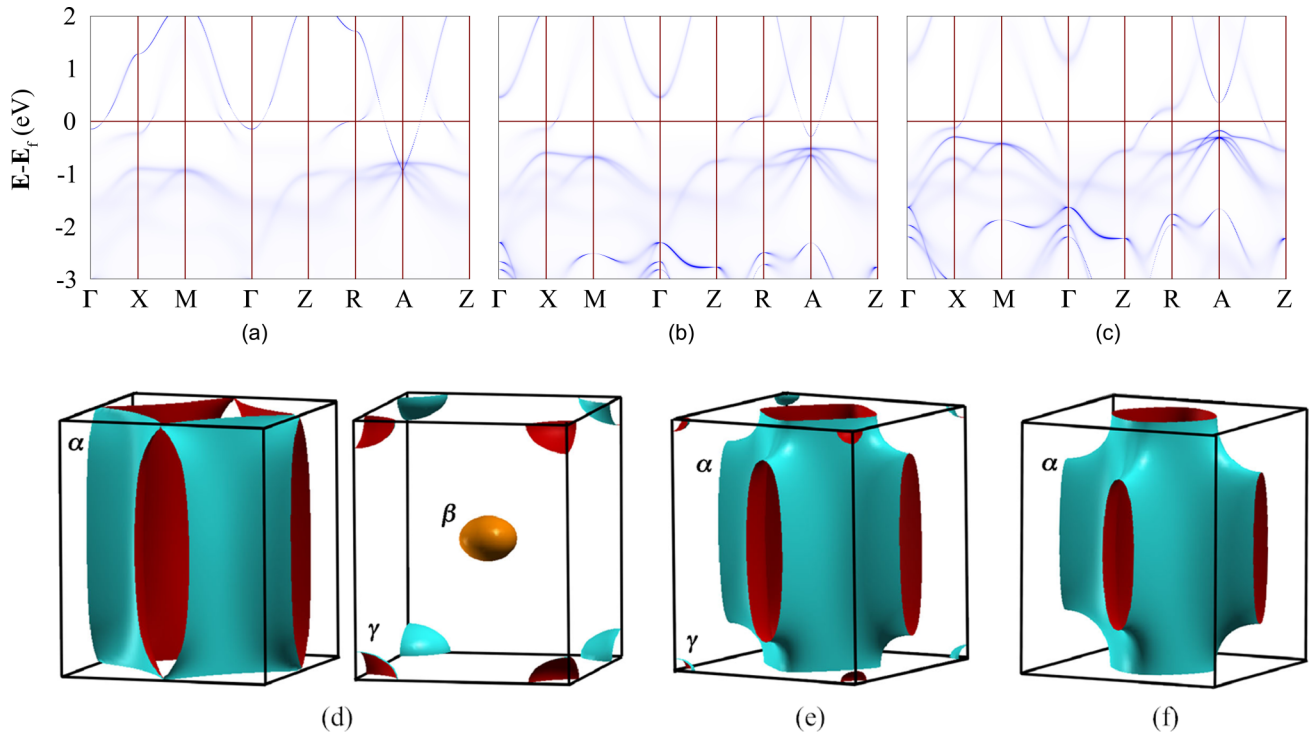


FIG. 3. \mathbf{k} -resolved spectral function from DFT+DMFT calculations for (a) pristine, (b) 0.2 hole-doped, and (c) 0.4 hole-doped NdNiO₂ at 116 K. DFT+DMFT Fermi surfaces of (d) pristine NdNiO₂, (e) 0.2 hole-doped NdNiO₂, and (f) 0.4 hole-doped NdNiO₂ from $V_{dc} = 47.4$ eV calculations. For clarity purposes, the dominating α sheet is separated from β and γ pockets in panel (d).

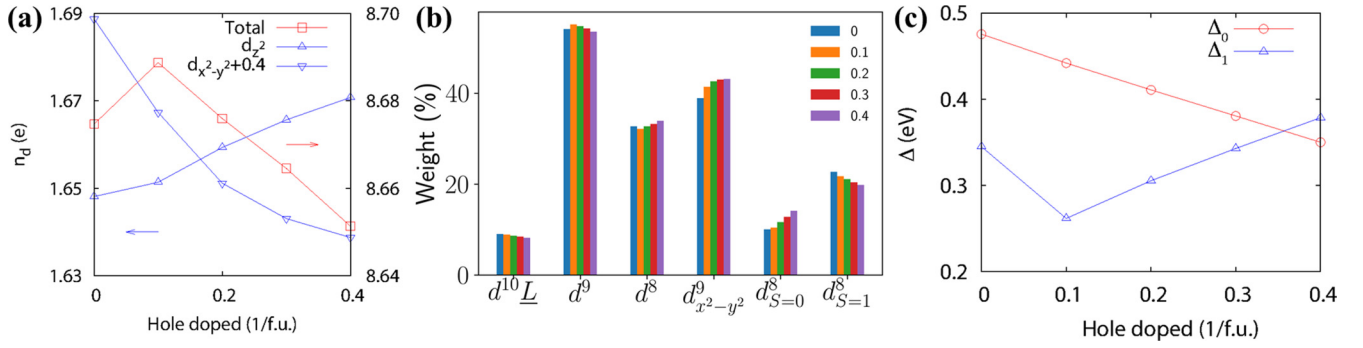


FIG. 4. Evolution of (a) Ni-3d e_g orbital occupation, (b) weight of many-body states, and (c) Ni-3d orbital crystal field splitting under hole doping. In panel (a), the occupation of $d_{x^2-y^2}$ is increased by 0.4 to fit in the plot. In panel (b), $d_{x^2-y^2}^9$ indicates d^9 state with unpaired $d_{x^2-y^2}$ electron, $d_{S=0}^8/d_{S=1}^8$ are d^8 spin-singlet/spin-triplet states, respectively. In panel (c), Δ_0 (Δ_1) are the energy differences between $d_{x^2-y^2}$ ($d_{zx/zy}$) and d_{xy} orbitals, respectively.

small. In other words, the Fermi level is pinned to the α sheet. Considering the fact that the α sheet is mainly contributed by the Ni $d_{x^2-y^2}$ orbital, such a Fermi surface pinning by the Ni $d_{x^2-y^2}$ orbital leads to two results: (1) The charge transfer energy between Ni $d_{x^2-y^2}$ and O-2p is reduced since O-2p experiences a large blue shift [as shown in Fig. 2(f)] [50]. Such a decrease in charge transfer energy in NiO₂ plane indicates more contributions from O-2p orbitals in the Fermi level, which may explain the existence of “shoulder” structure in the O-K edge resolved by electron energy loss spectroscopy (EELS) recently [51]. (2) The splitting between Ni $d_{x^2-y^2}$ and other Ni d orbitals becomes smaller, which drives NdNiO₂ towards multiorbital Hund’s physics [52].

We note that the above features upon doping are quite robust since similar behavior has been repeated with the strongly constrained and appropriately normed (SCAN) functional (see Appendix A). In addition, vanishingly small DOS of Sr is identified around the Fermi level, and therefore Sr doping does not introduce any Sr orbitals near the Fermi level. Thus, it is valid to ignore the chemical differences by removing valence electrons while simulating the doping effect.

B. DFT + DMFT results

We now turn to many-body results from DFT+DMFT calculations. In Figs. 3(a)–3(c), we present the \mathbf{k} -resolved spectral function for pristine, 0.2 hole doped, and 0.4 hole doped NdNiO₂ from DFT+DMFT calculations. Despite of the relatively high temperature (116 K), the electron states in the pristine compound are already very coherent near the Fermi level, in accordance with previous reports [9,53]. The spectral function of the pristine compound is quite similar to the DFT band structure, giving rise to three sheets of Fermi surfaces with similar shapes. Hole doping quickly suppresses the β pocket, which disappears with less than 0.1 hole doping. Therefore, this Nd- d_{z^2} /Ni- d_{z^2} derived pocket may be irrelevant to the superconductivity. The γ pocket is also substantially reduced by hole doping and eventually disappears around 0.3 hole doping. The largest α pocket is only moderately affected before 0.3 hole doping, due to its large volume and partial flat band close to the Fermi level at R . Further hole doping also causes substantial blue shift of the α pocket. We show the calculated DMFT Fermi surfaces in

Figs. 3(d)–3(f). In the pristine compound, the occupation of α , β , and γ pockets are 0.98 holes, 0.03 electrons, and 0.02 electrons, respectively. Upon 0.2 hole doping, the occupations of α and γ pockets are 1.19 holes and <0.01 electrons, respectively, while the β pocket disappears. In the 0.4 hole doped compound, only the α pocket remains with 1.32 hole occupation. Such observation is also consistent with the above DFT analysis and follows the Luttinger theorem. Moreover, as a result of the large blue shift of β and γ pockets upon hole doping, as well as the pinning of the α pocket due to Ni-3d $d_{x^2-y^2}$, the hybridization between the itinerant electrons and local Ni-3d orbitals reduces, resulting in sharper quasiparticle behavior upon hole doping [compare Figs. 3(b) and 3(c) with Fig. 3(a) (see also Fig. 7)].

We then focus on the 3d orbital occupations of the Ni atom [Fig. 4(a), also Table I]. The total Ni-3d occupation in the pristine compound is 8.675 e , and thus the Ni atom is valence fluctuating between Ni²⁺ (d^8) and Ni⁺ (d^9). Despite of the consistent and significant changes in the spectral function due to hole doping, the doping effect to orbital occupations clearly exhibits different behaviors for small and large doping ranges. Surprisingly, for small hole doping (<0.1 hole/cell), the overall Ni-3d occupation even increases. Once the hole doping exceeds 0.1 hole/cell, the overall Ni-3d occupations follow a consistent linear decreasing behavior with respect to the hole-doping level. Closer examination reveals further details. Among the 5 Ni-3d orbitals, the t_{2g} orbitals are nearly fully occupied, and are less relevant to the electronic states near the Fermi level. Therefore, the t_{2g} orbitals are “frozen”

TABLE I. Ni-3d orbital occupations and effective masses in both pristine and hole doped compounds for $V_{dc} = 47.4$ eV. The numbers within the brackets are the effective mass of respective orbitals calculated using $m^*/m = 1/Z = 1 - \frac{\partial \text{Im}[\Sigma(i\omega_n)]}{\partial \omega_n} \Big|_{\omega_n \rightarrow 0}$.

Doping	$d_{x^2-y^2}$	d_{z^2}	$d_{zx/zy}$	d_{xy}
0.0	1.289 (2.40)	1.648 (1.26)	3.797 (1.25)	1.941 (1.30)
0.1	1.267 (2.58)	1.651 (1.28)	3.826 (1.27)	1.944 (1.32)
0.2	1.251 (2.43)	1.659 (1.26)	3.826 (1.27)	1.939 (1.32)
0.3	1.243 (2.43)	1.666 (1.29)	3.824 (1.28)	1.932 (1.33)
0.4	1.239 (2.06)	1.671 (1.29)	3.819 (1.29)	1.923 (1.31)

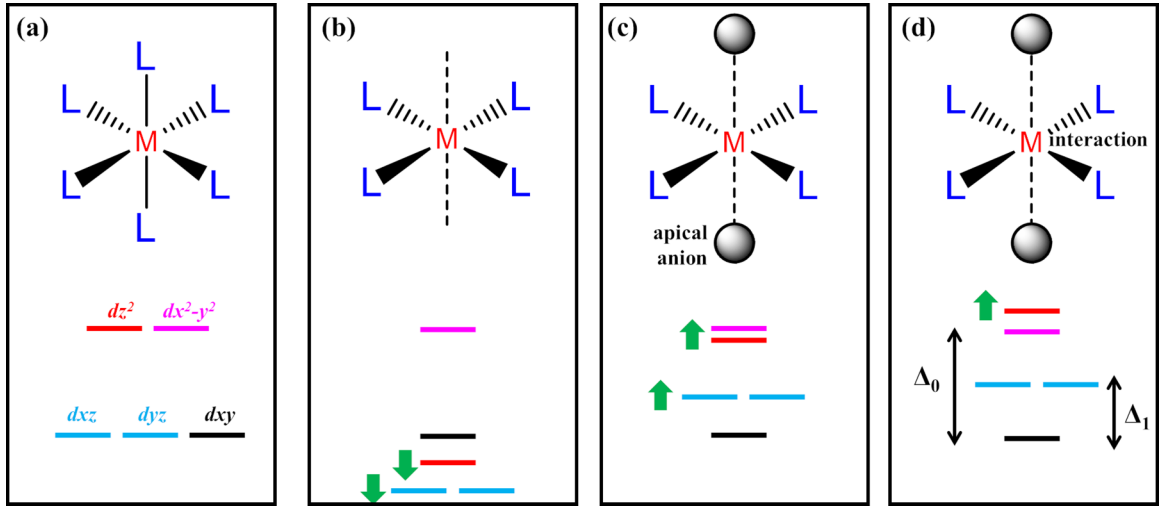


FIG. 5. Crystal field splitting of d orbitals with (a) O_h symmetry, (b) D_{4h} , (c) D_{4h} plus apical anions, and (d) D_{4h} plus apical anions with interaction. The d orbitals are labeled by different colors: $d_{x^2-y^2}$, d_{z^2} , d_{xz} (d_{yz}), and d_{xy} orbital corresponds to pink, red, blue, and black. The green filled arrows indicate how orbital order evolves with new effects.

during hole doping, although they cannot be ignored in the discussion of total d occupation. In the following discussion, we focus on the e_g orbitals [12,29,33,38]. The doped hole will populate on $d_{x^2-y^2}$, as the occupation decreases with hole doping as shown in Fig. 4(a). Interestingly, d_{z^2} occupation increases with hole doping. These findings are at odds with Ref. [32], where the hole mainly goes to d_{z^2} orbital. Such a charge correlation between d_{z^2} and $d_{x^2-y^2}$ agrees with the band shift upon hole doping from DFT calculations. In addition, the hole doping has a nontrivial effect on the effective mass of the Ni-3d orbitals as well. As shown in Table I, Ni-3d $_{x^2-y^2}$ orbital has the largest $m^*/m \approx 2.4$, and all other d orbitals show only mild correlation effect with m^*/m around 1.3 in the pristine compound. While the latter is less affected by hole doping, the effective mass of $d_{x^2-y^2}$, which is believed to be most relevant to the superconductivity, strongly depends on the doping. It ranges between 2.4 to 2.6 within 0.3 hole/cell doping, and suddenly drops to ≈ 2.1 with 0.4 hole/cell doping.

We also plot the statistical weight of sampled many-body states in Fig. 4(b). Again, we see clearly distinct hole-doping behavior for the small and large doping range. For the small doping range (< 0.1 hole/cell), the d^9 weight is significantly enhanced, primarily due to large increase of $d_{x^2-y^2}^9$ weight. Noticing that $d_{x^2-y^2}^9$ denotes d^9 with unpaired $d_{x^2-y^2}$, which is consistent with the reduced $d_{x^2-y^2}$ occupation due to hole doping. Beyond 0.1 hole/cell doping, the d^9 weight consistently drops, whereas the $d_{x^2-y^2}^9$ weight gradually reaches saturation around 43% at 0.4 hole/cell. Similarly, the d^8 configuration weight reduces from 32.7% to 32.1% in the small doping range, and then linearly increases to 33.9% at 0.4 hole/cell doping. Nevertheless, within the doping range we investigated, the weight of d^8 configuration is always more than three times larger than $d^{10}\underline{L}$, and even enhances with 0.4 hole doping. In a typical charge-transfer insulator, it is the weights of $d^{10}\underline{L}$ that should be comparable to that of d^9 rather than d^8 [29]. Thus, it suggests the multiorbital nature rather than charge transfer. Moreover, in the pristine and small doping

cases, the spin-triplet states always dominate the d^8 states (almost twice the weight of spin-singlet states). However, the weight ratio between spin-triplet and singlet states quickly reduces, and becomes close to 1 in the 0.4 hole/cell doped case. Therefore, Hund's physics is important in the pristine and lightly doped system but may lose its importance in the heavily doped compounds.

Such nonmonotonic doping effect is also observed for the crystal-field splitting of the Ni-3d electrons. Bare atomic level of Ni-3d orbitals (with respect to the Fermi level) can be obtained by fitting the undoped DFT result to a tight-binding Wannier Hamiltonian, which yields -1.398 , -1.459 , -1.676 , and -1.919 eV for $d_{x^2-y^2}$, d_{z^2} , $d_{zx/zy}$, and d_{xy} orbitals [Fig. 5(c)], respectively. The e_g orbitals are nearly degenerate and separated from t_{2g} by a large gap. Such crystal field splitting is consistent with the fact that the t_{2g} are “frozen” during hole doping. In the DFT+DMFT calculations, the electron density and energies are renormalized, and the orbitals order as $E(d_{z^2}) > E(d_{x^2-y^2}) > E(d_{zx/zy}) > E(d_{xy})$ [Fig. 5(d)] in the pristine compound. Since d_{z^2} has larger occupation than $d_{x^2-y^2}$, the orbital order flip between d_{z^2} and $d_{x^2-y^2}$ reflects the fact that $d_{x^2-y^2}$ has much larger onsite Hubbard repulsion than d_{z^2} , which renders the validity of the one-band Hubbard model [38]. Since $d_{x^2-y^2}$ occupation is larger than half-filled, the hole residue on $d_{x^2-y^2}$ will greatly stabilize the system, as found in Fig. 4(a). The observation of stronger correlation of $d_{x^2-y^2}$ than d_{z^2} is also in agreement with the fact that $d_{x^2-y^2}$ has a much larger effect mass than d_{z^2} . Normally, for D_{4h} symmetry without apical anions, crystal field splitting leads to lowest $d_{zx/zy}$, d_{z^2} instead of d_{xy} orbitals [see Fig. 5(b)]. However, the NdNiO₂ compound stems from NdNiO₃ crystal, where the octahedral crystal field leads to degenerate t_{2g} and e_g splittings for Ni-3d orbitals [see Fig. 5(a)]. Once the apical O²⁻ anions are removed, negative charge occupation accumulates at the apical oxygen position [4,34], and thus orbitals extending along the z direction cost energy, raising energies of d_{z^2} , d_{zx} , and d_{zy} orbitals. Therefore, the d_{xy} orbital becomes the lowest lying component. The $d_{zx/zy}$ orbitals are less affected than the

d_{z^2} , and therefore are also low lying and nearly fully occupied. This is just what we obtained from DFT results. Such an orbital order will change with the inclusion of interaction as in our DFT+DMFT calculations. The $d_{x^2-y^2}$ is the most correlated one and its orbital energy is even lower than d_{z^2} . Such a orbital order flip has also been reported in a recent GW+DMFT study [54]. In such distorted octahedral crystal field, the original octahedral crystal-field splitting is characterized by the energy difference between $d_{x^2-y^2}$ and d_{xy} orbitals $\Delta_0 = E(d_{x^2-y^2}) - E(d_{xy})$ [see Fig. 5(d)], and the effect of distortion is reflected in the energy difference between d_{xy} and $d_{zx/zy}$ orbitals $\Delta_1 = E(d_{zx/zy}) - E(d_{xy})$ [see Fig. 5(d)]. We plot the doping-dependent Δ_0 and Δ_1 in Fig. 4(c). Throughout the hole doping range, Δ_0 exhibits linear dependence on the doping level, but Δ_1 decreases below 0.1 hole doping and then quickly linearly increases with further hole doping. This leads to an inversion between $d_{x^2-y^2}$ and $d_{zx/zy}$ at 0.4 hole doping.

Finally, we address the effect of the undetermined double-counting term. The above reported results were obtained using a fixed double-counting $V_{dc} = 47.4$ eV (or equivalently nominal $n^0 = 9.0$), which leads to actual n^d close to 8.6. An $n^d = 9.0$ solution can be achieved by using $V_{dc} = 51.84$ eV. In this case, the β pocket disappears even in the pristine compound, and the size of γ pocket is drastically reduced compared to the above results. Hole doping in this case will quickly suppress the γ pocket, leaving only the α pocket in the BZ. The $d^{10}\bar{L}$ configuration weight is much enhanced and can be comparable to the d^8 weight (Table III). In this case, the hole doping quickly suppress the effect of Hund's rule, and the weight of spin-singlet states are comparable to the spin-triplet states as early as 0.2 hole/cell doping. Nevertheless, the aforementioned nonmonotonic doping effect to the d -orbital occupation, many-body configuration weight, crystal-field splitting, and effective mass still remains (Fig. 8

and Tables II and III). Thus, our results are robust with respect to the choice of double-counting terms.

IV. DISCUSSION

We have performed a systematic study of electronic properties of the normal state of NdNiO₂ by DFT and DMFT methods. The complementary methods show the normal state of hole-doped NdNiO₂ as a valence-fluctuating correlated metal. Hund's effect and the hybridization effect gradually are reduced by increasing the doping level. Importantly, we identify a nonmonotonic many-body doping effect on Ni-3d orbitals, as evidenced by the electron occupation, orbital crystal field splitting, and statistical spectral weight of orbital configurations. Additionally, the doping effect leads to the change of topology of Fermi surface and reduction of correlations, which could be relevant to the underlying superconductivity [22].

We would like make several remarks here. First of all, our results show that the normal state of doped NdNiO₂ is quite different from the copper oxide superconductors; instead it is closer to the iron-based superconductors where multiorbital physics dominates. Second, we identify Ni-3d_{x²-y²} orbital as the most correlated one, which should be helpful for building the effective model. Third, some features shown here could provide plausible understanding for experimental observations. For example, both DFT and DFT+DMFT calculations (Figs. 2 and 3) show the O-2p state moving toward the Fermi level upon Sr doping, which is consistent with a recent EELS study on the O-K edge that gives a shoulder structure, pointing to the Ni-O singlet state [51]. Finally, we argue that the Nd f electrons influence the electronic states below the Fermi energy, leaving the physics close to the Fermi level unaffected. In addition, the occupations and effective masses of Ni-3d orbitals in both pristine and hole-doped compounds are qualitatively

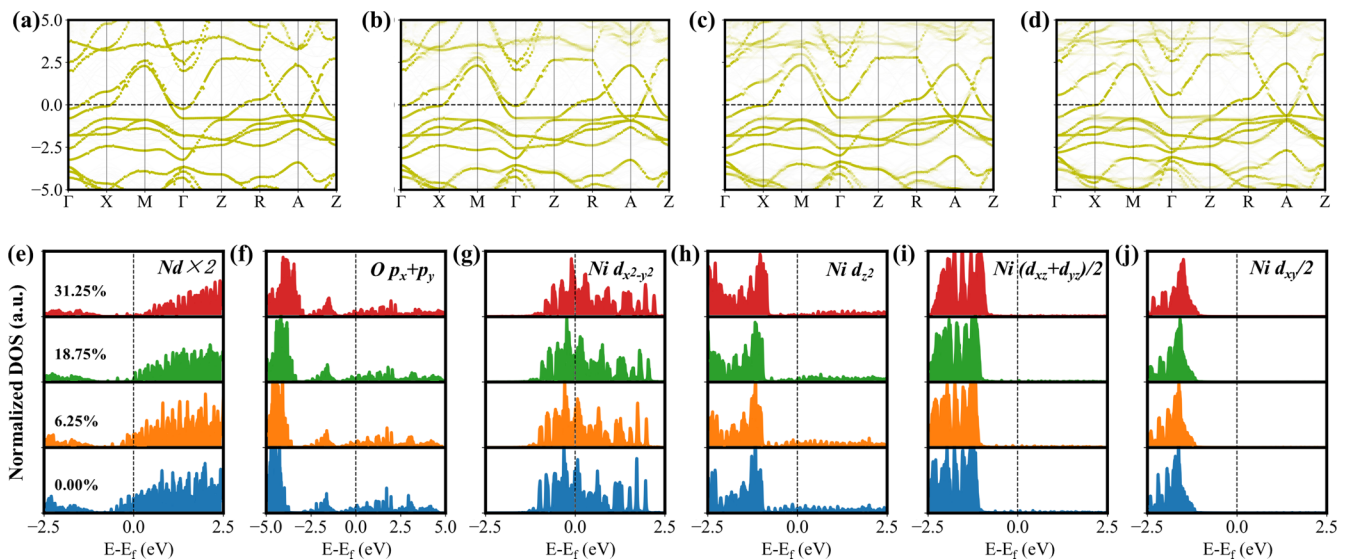


FIG. 6. [(a)–(d)] Unfolded band structures for different Sr doping concentration. From left to right: $\delta = 0.00\%$, 6.25% , 18.75% , and 31.25% . [(e)–(j)] Projected density of state with different δ on different subspaces with arbitrary unit (a.u.), from left to right: Nd atoms, O p_{x+y} , Ni $d_{x^2-y^2}$, Ni d_{z^2} , Ni $d_{xz} + d_{yz}$, and Ni d_{xy} orbitals. The weights in panels (a), (e), and (f) have been rescaled by factors of 2, 1/2, and 1/2. From bottom to top, δ increases from 0.00% to 31.25% in each panel.

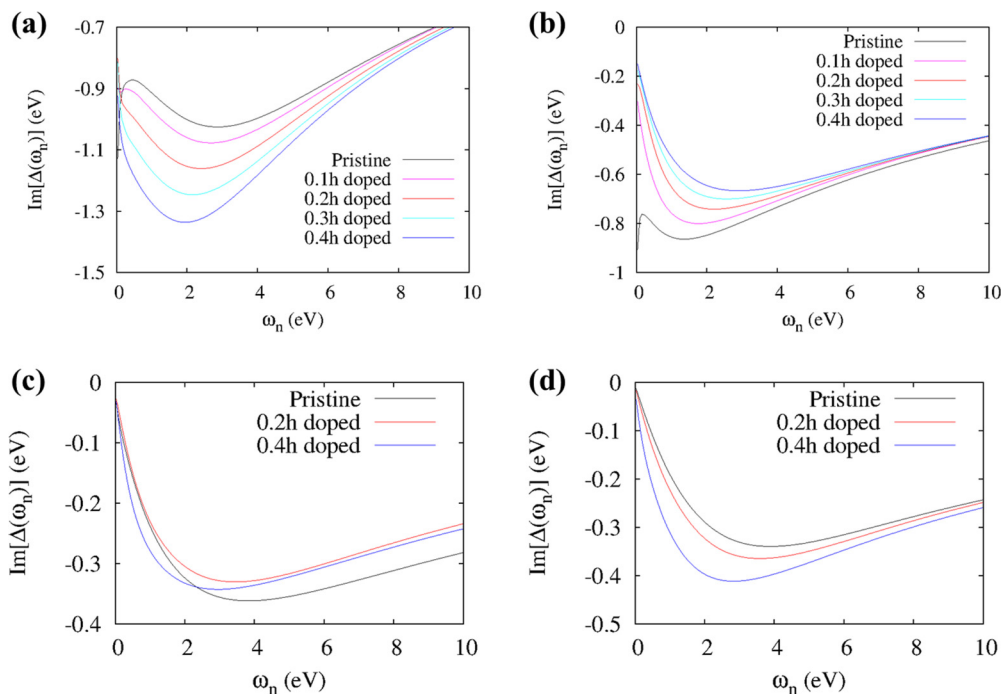


FIG. 7. Doping dependence of hybridization function for (a) Ni-3d_{x²-y²}, (b) Ni-3d_{z²}, (c) Ni-3d_{zx/zy}, and (d) Ni-3d_{xy} orbitals in $V_{dc} = 47.4$ eV calculations.

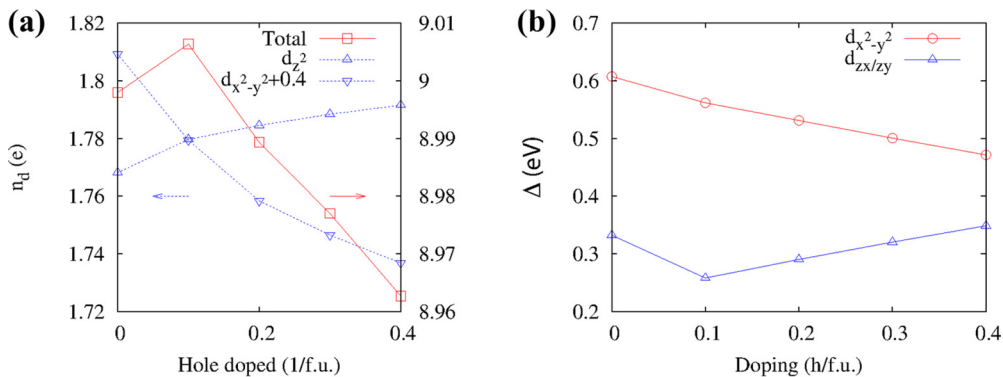


FIG. 8. Evolution of (a) Ni-3d orbital occupation and (b) Ni-3d orbital crystal field splitting under hole doping, calculated using $V_{dc} = 51.84$ eV.

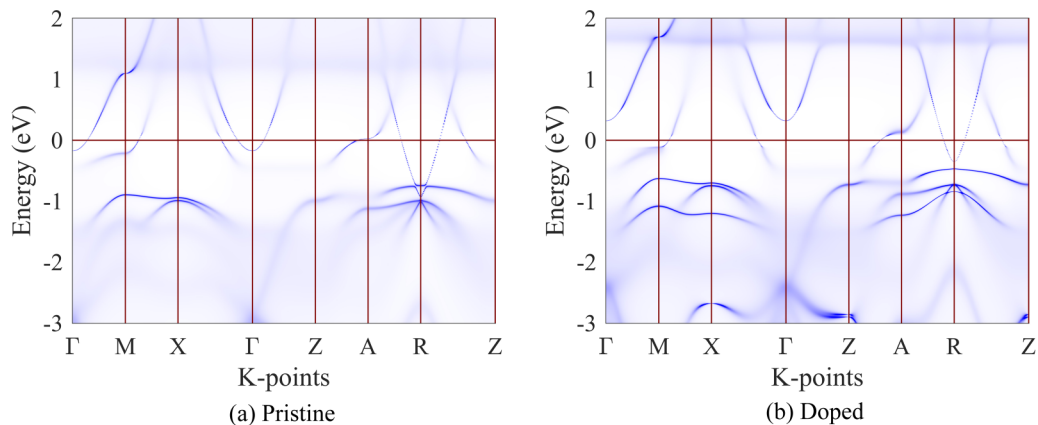


FIG. 9. **k**-resolved spectral function from DFT+DMFT calculations, by including *f* electrons.

TABLE II. Ni-3*d* orbital occupations and effective masses in both pristine and hole doped compounds for $V_{dc} = 51.84$ eV. The numbers within the brackets are the effective masses of the respective orbitals.

Doping	$d_{x^2-y^2}$	d_{z^2}	$d_{zx/zy}$	d_{xy}
0.0	1.409 (1.78)	1.768 (1.20)	3.860 (1.20)	1.960 (1.23)
0.1	1.379 (1.85)	1.780 (1.20)	3.884 (1.20)	1.963 (1.23)
0.2	1.358 (1.84)	1.785 (1.20)	3.885 (1.20)	1.962 (1.24)
0.3	1.346 (1.79)	1.788 (1.20)	3.883 (1.20)	1.959 (1.23)
0.4	1.337 (1.74)	1.792 (1.21)	3.880 (1.20)	1.954 (1.23)

similar to the case without f electrons. These arguments are supported by our full-electron calculation of NdNiO₂ by explicitly including Nd-4*f* orbitals (see Appendix C, Table IV, and Fig. 9). These results all indicate the f electrons may be irrelevant in NdNiO₂, in good agreement with the existing experiment [55].

Recently, we have become aware of other works using GW+DMFT [54] and DFT+DMFT [56,57].

ACKNOWLEDGMENTS

The authors thanks J.-X. Zhu, Zhi Ren, and H. H. Wen for inspiring and helpful discussions. This work was supported by NSFC (Grants No. 11774325, No. 11874137, No. 21603210, No. 21603205, and No. 21688102), National Key Research and Development Program of China (Grants No. 2017YFA0204904 and No. 2016YFA0200600), Anhui Initiative in Quantum Information Technologies (Grant No. AHY090400), Fundamental Research Funds for the Central Universities, and the Start-up Funding from Westlake University. We thank Supercomputing Center at USTC for providing the computing resources. DMFT calculations were performed on the High Performance Computing Cluster at Hangzhou Normal University and at the Beijing Supercloud Computing Center.

APPENDIX A: ADDITIONAL RESULTS OF DFT

Since NdNiO₂ belongs to transition metal oxide materials, exchange-correlation functionals like PBE will always underestimate the band gap. To improve the validity of our DFT calculations, exchange-correlation functionals in higher stairs of Jacob's ladder [58] are useful. One possibility is the hybrid exchange correlation functionals such as B3LYP or B3PW, which have reproduced band gaps of transition metal oxide materials in excellent agreement with the experiments [59,60]. The other possibility is the meta-GGA. The recently developed SCAN functional [61] makes it possible to treat charge, spin, and lattice degrees of freedom on equal footing. As a parameter-free functional, SCAN has shown great success in different types of bonding systems [62], even in cuprates [63–65], which is believed to be the typical strongly correlated system. Therefore, we also use SCAN functional to study the effect of Sr doping.

The unfolded band structure at $\delta = 0.00\%$, 6.25% , 18.75% , and 31.25% is shown in Figs. 6(a)–6(d). Similar to the result

TABLE III. Statistical weights of many-body configurations in pristine and doped compounds for $V_{dc} = 51.84$ eV.

Doping	$d^{10}\underline{L}$	d^9	$d_{x^2-y^2}^9$	$d_{s=0}^8$	$d_{s=1}^8$
0.0	21.4%	58.5%	41.9%	6.4%	12.1%
0.1	21.2%	59.5%	45.3%	6.8%	11.1%
0.2	20.3%	59.7%	46.9%	7.5%	11.0%
0.3	19.8%	59.7%	47.8%	8.1%	10.9%
0.4	19.2%	59.5%	48.3%	8.9%	10.8%

of PBE, the evolution of electronic structure upon hole doping is non-rigid-like: (1) The β pocket undergoes Lifshitz transition at a low δ around 6.25% . (2) The γ pocket does not vanish even at $\delta = 31.25\%$. (3) The α sheet pins the Fermi level. The projected density of state is shown in Figs. 6(e)–6(j). In accordance with PBE, the SCAN functional gives similar results on the evolution of electronic structure with hole doping.

APPENDIX B: ADDITIONAL RESULTS OF DMFT

In Fig. 7, we show the hybridization function in Matsubara frequency from DFT+DMFT calculations. In pristine compounds, both Ni-3*d* _{x^2-y^2} and Ni-3*d* _{z^2} orbitals show strong hybridization with the conduction electrons, as indicated by their divergent behavior with $\omega_n \rightarrow 0$. A small doping with 0.1 hole quickly suppresses the divergent behavior of both orbitals. The doping effect on t_{2g} orbital hybridization functions is much less prominent.

In Table I, we show the orbital occupation and effective masses in both pristine and doped compounds, calculated with $V_{dc} = 47.4$ eV. A decrease of $d_{x^2-y^2}$ effective mass from 0.1 hole/cell doping to 0.4 hole/cell doping can be observed, and a sudden drop from 0.3 hole/cell doping to 0.4 hole/cell doping can be identified. A similar decrease of d_{z^2} effective mass can also be identified in $V_{dc} = 51.84$ eV calculations (Table II); however, the sudden drop from 0.3 to 0.4 hole/cell doping is absent in $V_{dc} = 51.84$ eV calculations.

In Table III, we show the statistic weight of sampled many-body configurations in the pristine and doped compounds for $V_{dc} = 51.84$ eV. Although the $d^{10}\underline{L}$ configuration weight is substantially higher than $V_{dc} = 47.4$ eV calculations, the nonmonotonic doping effect can still be observed. Similarly, the nonmonotonic doping effect can also be identified from the Ni-3*d* occupation and crystal field splittings in $V_{dc} = 51.84$ eV calculations (Fig. 8).

TABLE IV. In a calculation with f electrons, 3*d*-orbital occupations and effective masses in both pristine and 0.2 hole doped compounds. The numbers within the brackets are the effective mass of respective orbitals.

Doping	$d_{x^2-y^2}$	d_{z^2}	$d_{zx/zy}$	d_{xy}
0.0	1.271 (2.30)	1.631 (1.23)	3.775 (1.21)	1.942 (1.23)
0.2	1.236 (2.28)	1.628 (1.24)	3.806 (1.23)	1.945 (1.24)

APPENDIX C: ELECTRONIC STRUCTURE WITH f ELECTRONS

In this part, we show the results from DFT+DMFT calculation explicitly considering Nd- $4f$ electrons in Fig. 9. These calculations are done with $U_f = 6.0$ eV, $J_f = 0.7$ eV on Nd- $4f$ orbitals and $U_d = 5.0$ eV, $J_d = 0.8$ eV on Ni- $3d$

orbitals. As shown in Fig. 3, the \mathbf{k} -resolved spectral functions are almost the same with as the calculations without f electrons. In addition, the $3d$ -orbital occupation and effective masses are also qualitatively the same (see Table IV). Since the calculations are extremely expensive due to Nd- $4f$ orbitals, we have only calculated pristine and 0.2 hole doped compounds.

-
- [1] D. Li, K. Lee, B. Y. Wang, M. Osada, S. Crossley, H. R. Lee, Y. Cui, Y. Hikita, and H. Y. Hwang, *Nature (London)* **572**, 624 (2019).
- [2] A. S. Botana and M. R. Norman, *Phys. Rev. X* **10**, 011024 (2020).
- [3] H. Sakakibara, H. Usui, K. Suzuki, T. Kotani, H. Aoki, and K. Kuroki, *Phys. Rev. Lett.* **125**, 077003 (2020).
- [4] Y. Nomura, M. Hirayama, T. Tadano, Y. Yoshimoto, K. Nakamura, and R. Arita, *Phys. Rev. B* **100**, 205138 (2019).
- [5] P. Jiang, L. Si, Z. Liao, and Z. Zhong, *Phys. Rev. B* **100**, 201106(R) (2019).
- [6] M. Hepting, D. Li, C. Jia, H. Lu, E. Paris, Y. Tseng, X. Feng, M. Osada, E. Been, Y. Hikita, Y.-D. Chuang, Z. Hussain, K. J. Zhou, A. Nag, M. Garcia-Fernandez, M. Rossi, H. Y. Huang, D. J. Huang, Z. X. Shen, T. Schmitt, H. Y. Hwang, B. Moritz, J. Zaanen, T. P. Devereaux, and W. S. Lee, *Nat. Mater.* **19**, 381 (2020).
- [7] G.-M. Zhang, Y.-F. Yang, and F.-C. Zhang, *Phys. Rev. B* **101**, 020501(R) (2020).
- [8] Z. Liu, Z. Ren, W. Zhu, Z. F. Wang, and J. Yang, *npj Quantum Mater.* **5**, 31 (2020).
- [9] I. Leonov, S. L. Skornyakov, and S. Y. Savrasov, *Phys. Rev. B* **101**, 241108(R) (2020).
- [10] M.-Y. Choi, W. E. Pickett, and K.-W. Lee, *Phys. Rev. Research* **2**, 033445 (2020).
- [11] I. Leonov and S. Y. Savrasov, [arXiv:2006.05295](https://arxiv.org/abs/2006.05295).
- [12] X. Wan, V. Ivanov, G. Resta, I. Leonov, and S. Y. Savrasov, [arXiv:2008.07465](https://arxiv.org/abs/2008.07465).
- [13] M. Jiang, M. Berciu, and G. A. Sawatzky, *Phys. Rev. Lett.* **124**, 207004 (2020).
- [14] X. Wu, D. Di Sante, T. Schwemmer, W. Hanke, H. Y. Hwang, S. Raghu, and R. Thomale, *Phys. Rev. B* **101**, 060504(R) (2020).
- [15] Y.-H. Zhang and A. Vishwanath, *Phys. Rev. Res.* **2**, 023112 (2020).
- [16] P. Werner and S. Hoshino, *Phys. Rev. B* **101**, 041104(R) (2020).
- [17] L.-H. Hu and C. Wu, *Phys. Rev. Res.* **1**, 032046(R) (2019).
- [18] J. Chang, J. Zhao, and Y. Ding, *Eur. Phys. J. B* **93**, 220 (2020).
- [19] P. Adhikary, S. Bandyopadhyay, T. Das, I. Dasgupta, and T. Saha-Dasgupta, *Phys. Rev. B* **102**, 100501(R) (2020).
- [20] D. Li, B. Y. Wang, K. Lee, S. P. Harvey, M. Osada, B. H. Goodge, L. F. Kourkoutis, and H. Y. Hwang, *Phys. Rev. Lett.* **125**, 027001 (2020).
- [21] S. Zeng, C. S. Tang, X. Yin, C. Li, M. Li, Z. Huang, J. Hu, W. Liu, G. J. Omar, H. Jani, Z. S. Lim, K. Han, D. Wan, P. Yang, S. J. Pennycook, A. T. S. Wee, and A. Ariando, *Phys. Rev. Lett.* **125**, 147003 (2020).
- [22] Q. Gu, Y. Li, S. Wan, H. Li, W. Guo, H. Yang, Q. Li, X. Zhu, X. Pan, Y. Nie, and H.-H. Wen, *Nat. Commun.* **11**, 6027 (2020).
- [23] H. Romberg, M. Alexander, N. Nücker, P. Adelman, and J. Fink, *Phys. Rev. B* **42**, 8768 (1990).
- [24] P. W. Anderson, *Science* **235**, 1196 (1987).
- [25] P. A. Lee, N. Nagaosa, and X.-G. Wen, *Rev. Mod. Phys.* **78**, 17 (2006).
- [26] F. C. Zhang and T. M. Rice, *Phys. Rev. B* **37**, 3759 (1988).
- [27] M. Ogata and H. Fukuyama, *Rep. Prog. Phys.* **71**, 036501 (2008).
- [28] Z.-J. Lang, R. Jiang, and W. Ku, [arXiv:2005.00022](https://arxiv.org/abs/2005.00022).
- [29] J. Karp, A. S. Botana, M. R. Norman, H. Park, M. Zingl, and A. Millis, *Phys. Rev. X* **10**, 021061 (2020).
- [30] H. Zhang, L. Jin, S. Wang, B. Xi, X. Shi, F. Ye, and J.-W. Mei, *Phys. Rev. Res.* **2**, 013214 (2020).
- [31] V. Olevano, F. Bernardini, X. Blase, and A. Cano, *Phys. Rev. B* **101**, 161102(R) (2020).
- [32] F. Lechermann, *Phys. Rev. B* **101**, 081110(R) (2020).
- [33] F. Lechermann, *Phys. Rev. X* **10**, 041002 (2020).
- [34] Y. Gu, S. Zhu, X. Wang, J. Hu, and H. Chen, *Commun. Phys.* **3**, 84 (2020).
- [35] Z. Wang, G.-M. Zhang, Y.-F. Yang, and F.-C. Zhang, *Phys. Rev. B* **102**, 220501(R) (2020).
- [36] R. Zhang, C. Lane, B. Singh, J. Nokelainen, B. Barbiellini, R. S. Markiewicz, A. Bansil, and J. Sun, [arXiv:2009.05816](https://arxiv.org/abs/2009.05816).
- [37] R. He, P. Jiang, Y. Lu, Y. Song, M. Chen, M. Jin, L. Shui, and Z. Zhong, *Phys. Rev. B* **102**, 035118 (2020).
- [38] M. Kitatani, L. Si, O. Janson, R. Arita, Z. Zhong, and K. Held, *npj Quantum Mater.* **5**, 59 (2020).
- [39] M.-Y. Choi, K.-W. Lee, and W. E. Pickett, *Phys. Rev. B* **101**, 020503(R) (2020).
- [40] J.-C. Gao, S. Peng, Z.-J. Wang, C. Fang, and H.-M. Weng, *Nat. Sci. Rev.*, [nwaa218](https://doi.org/10.1093/nsr/nwaa218) (2020), doi: 10.1093/nsr/nwaa218.
- [41] M. P. Teter, M. C. Payne, and D. C. Allan, *Phys. Rev. B* **40**, 12255 (1989).
- [42] G. Kresse and J. Furthmüller, *Phys. Rev. B* **54**, 11169 (1996).
- [43] P. E. Blöchl, *Phys. Rev. B* **50**, 17953 (1994).
- [44] J. P. Perdew, K. Burke, and M. Ernzerhof, *Phys. Rev. Lett.* **77**, 3865 (1996).
- [45] U. Herath, P. Tavadze, X. He, E. Bousquet, S. Singh, F. Muñoz, and A. H. Romero, *Comput. Phys. Commun.* **251**, 107080 (2020).
- [46] K. Haule, C.-H. Yee, and K. Kim, *Phys. Rev. B* **81**, 195107 (2010).
- [47] P. Blaha, K. Schwarz, F. Tran, R. Laskowski, G. K. H. Madsen, and L. D. Marks, *J. Chem. Phys.* **152**, 074101 (2020).
- [48] L. Bellaïche and D. Vanderbilt, *Phys. Rev. B* **61**, 7877 (2000).
- [49] E. Gull, A. J. Millis, A. I. Lichtenstein, A. N. Rubtsov, M. Troyer, and P. Werner, *Rev. Mod. Phys.* **83**, 349 (2011).
- [50] J. Kirshna, H. LaBollita, A. O. Fumega, V. Pardo, and A. S. Botana, *Phys. Rev. B* **102**, 224506 (2020).
- [51] B. H. Goodge, D. Li, M. Osada, B. Y. Wang, K. Lee, G. A. Sawatzky, H. Y. Hwang, and L. F. Kourkoutis, [arXiv:2005.02847](https://arxiv.org/abs/2005.02847).

- [52] A. Georges, L. de' Medici, and J. Mravlje, *Annu. Rev. Condens. Matter Phys.* **4**, 137 (2013).
- [53] S. Ryee, H. Yoon, T. J. Kim, M. Y. Jeong, and M. J. Han, *Phys. Rev. B* **101**, 064513 (2020).
- [54] F. Petocchi, V. Christiansson, F. Nilsson, F. Aryasetiawan, and P. Werner, *Phys. Rev. X* **10**, 041047 (2020).
- [55] M. Osada, B. Y. Wang, B. H. Goodge, K. Lee, H. Yoon, K. Sakuma, D. Li, M. Miura, L. F. Kourkoutis, and H. Y. Hwang, *Nano Lett.* **20**, 5735 (2020).
- [56] Y. Wang, C.-J. Kang, H. Miao, and G. Kotliar, *Phys. Rev. B* **102**, 161118(R) (2020).
- [57] B. Kang, C. Melnick, P. Semon, G. Kotliar, and S. Choi, *arXiv:2007.14610*.
- [58] J. P. Perdew, A. Ruzsinszky, J. Tao, V. N. Staroverov, G. E. Scuseria, and G. I. Csonka, *J. Chem. Phys.* **123**, 062201 (2005).
- [59] R. I. Eglitis and A. I. Popov, *J. Saudi Chem. Soc.* **22**, 459 (2018).
- [60] R. I. Eglitis, J. Purans, J. Gabrusenoks, A. I. Popov, and R. Jia, *Crystals* **10**, 745 (2020).
- [61] J. Sun, A. Ruzsinszky, and J. P. Perdew, *Phys. Rev. Lett.* **115**, 036402 (2015).
- [62] J. Sun, R. C. Remsing, Y. Zhang, Z. Sun, A. Ruzsinszky, H. Peng, Z. Yang, A. Paul, U. Waghmare, X. Wu, M. L. Klein, and J. P. Perdew, *Nat. Chem.* **8**, 831 (2016).
- [63] C. Lane, J. W. Furness, I. G. Buda, Y. Zhang, R. S. Markiewicz, B. Barbiellini, J. Sun, and A. Bansil, *Phys. Rev. B* **98**, 125140 (2018).
- [64] J. W. Furness, Y. Zhang, C. Lane, I. G. Buda, B. Barbiellini, R. S. Markiewicz, A. Bansil, and J. Sun, *Commun. Phys.* **1**, 11 (2018).
- [65] Y. Zhang, C. Lane, J. W. Furness, B. Barbiellini, J. P. Perdew, R. S. Markiewicz, A. Bansil, and J. Sun, *Proc. Natl. Acad. Sci. USA* **117**, 68 (2020).